Quarterly Journal of the Royal Meteorological Society

Q. J. R. Meteorol. Soc. **136**: 718–739, April 2010 Part A

RMetS

Royal Meteorological Society

Measurement and simulation of mid- and far-infrared spectra in the presence of cirrus

C. V. Cox[a]*, J. E. Harries[a], J. P. Taylor[b†], P. D. Green[a], A. J. Baran[b†], J. C. Pickering[a], A. E. Last[a] and J.E. Murray[a]

[a]*Department of Space and Atmospheric Physics, Imperial College, London, UK*
[b]*Met Office, Exeter, UK*

*Correspondence to: C. V. Cox, Space Science and Technology Department, Science and Technology Facilities Council, Rutherford Appleton Laboratory, Harwell Science and Innovation Campus, Didcot OX11 0QX, Oxon, UK.
E-mail: caroline.cox@stfc.ac.uk*

[†]The contributions of Taylor and Baran were written in the course of their employment at the Met Office, UK, and are published with the permission of the Controller of HMSO and the Queen's Printer for Scotland.

Observed far-infrared and mid-infrared radiance spectra measured *in situ* above cirrus with both the Tropospheric Airborne Fourier Transform Spectrometer (TAFTS) and the Airborne Research Interferometer Evaluation System (ARIES) are presented. Two sets of upwelling spectra between wavenumbers 100 and 1415cm^{-1} taken over ice cloud of visible optical thickness 0.1 and 0.3 are shown. These observations address the need for more measurements of radiance from cirrus, particularly in the far infrared, where experimental data are lacking. A test of consistency in modelling in both the far infrared and mid infrared is performed by fitting a model calculation of radiances in the infrared window region, and comparing with the measured radiances. In this consistency check, the sampling of the surrounding atmosphere and the cloud is given extensive consideration. The model was not able to consistently reproduce the observed radiance across the entire region, and was particularly poor in the 330–600cm^{-1} region of the far infrared. Possible causes are thought to be primarily model input uncertainties arising from inadequate sampling of cloud and atmosphere. Copyright © 2010 Royal Meteorological Society and Crown Copyright.

1. Introduction

Cirrus clouds have a pronounced effect on the total outgoing long-wave radiation of the Earth due to their ice particle composition, height in the atmosphere and ubiquitous nature, covering 30% of the globe (Liou, 1986). The magnitude and sign of their overall radiative effect is sensitive not only to altitude and optical thickness, but also to the cloud microphysics (Baker, 1997; Zhang *et al.*,
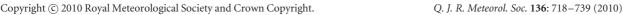
1999). Ice crystals that make up cirrus can take a variety of shapes (Lynch *et al.*, 2002), making modelling of the radiative transfer difficult. The calculated ice single scattering properties, produced by approximation theories, require validation by comparing modelled spectra with measured spectra. A number of studies have done this by looking for consistency in the solar and mid-infrared (MIR) spectral regions, e.g. Francis *et al.* (1999) and Baran and Francis (2004), and several theoretical studies have been performed

on the response of the far infrared (FIR) to variations in cirrus microphysics (Yang *et al.*, 2003; Baran, 2005). However, these theoretical studies have not been validated experimentally for the FIR.

The FIR is an important spectral region to study (Harries *et al.*, 2008). A significant proportion (up to one third) of the cooling of the Earth to space takes place in the FIR region from the mid and upper troposphere (Sinha and Harries, 1995), and the wavenumber where the peak of the Planck emission curve occurs is in the FIR also. The sensitivity of the FIR to variations in mid- to upper-tropospheric water vapour has already been measured (Cox *et al.*, 2007), and the current work extends this study to cirrus sensitivity. Since cirrus lies at such high altitudes in the mid to upper troposphere, and with the relatively high absorption of ice in the FIR, it is particularly important to be able to accurately model their effects in this spectral region. Indeed, the variation of the real and imaginary refractive indices of ice are such that we can expect strong scattering effects in the FIR, and therefore this region, together with the MIR and solar regions, may be useful for retrieving information on ice microphysics. Therefore it is vital that we are able to model radiance spectra consistently in the FIR and MIR.

Measurements of upwelling radiation taken above cirrus in both the FIR and MIR spectral regions, defined in this work as wavenumbers between 100 and 600 cm^{-1} and between 600 and 1415 cm^{-1} respectively, are presented. These measurements were made by the Tropospheric Airborne Fourier Transform Spectrometer (TAFTS; Canas *et al.*, 1997), measuring in the FIR, and the UK Met Office Airborne Research Interferometer Evaluation System (ARIES; Wilson *et al.*, 1999), measuring in the MIR, during the WINTEX campaign, a series of UK Met Office winter experiments flown from Cranfield, UK, between October 2004 and February 2005. On 11 February 2005, both instruments flew on board the UK Facility for Atmospheric Airborne Measurements (FAAM) BAE 146 aircraft, and sampled cirrus over the North Sea. On-board auxiliary instrumentation allowed the properties of both the atmosphere and cloud ice particles to be sampled for modelling purposes. Presented here are two sets of near-coincident TAFTS and ARIES upwelling spectra measured in the tops of cirrus, in two sections of cloud where the visible optical thickness was estimated to be around 0.3 and 0.1.

In this work, the simulation of the observed FIR TAFTS and MIR ARIES spectra has been considered in some detail, in order to demonstrate how the sampling and representation of an ice cloud may be addressed. The spectra have been simulated using measurements of cloud particle size distributions (PSDs) combined with theoretical single scattering properties of ice crystals. The measured PSDs have been adjusted to provide agreement with the measured spectra in the infrared window region (750–1250 cm^{-1}) and subsequently compared across the infrared region between 100 and 1415 cm^{-1}. Such an adjustment of the PSDs was performed as ice particles less than 25 μm were not measured by any instrumentation on board the FAAM aircraft, essentially retrieving the correct overall ice content of the cloud. This kind of study is complicated by both the movement of the cloud in the atmosphere, the movement of the aircraft with respect to the cloud and the potentially high spatial and temporal variability of ice cloud itself.
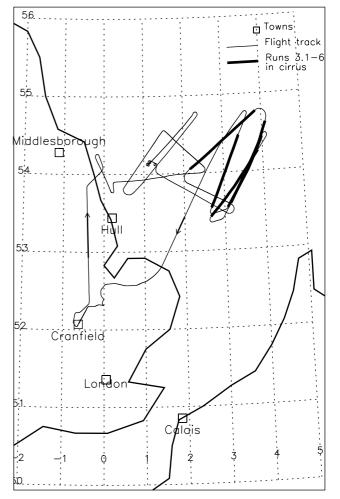

Figure 1. A plot of the flight track of the FAAM aircraft on 11 February 2005 when it sampled cirrus over the North Sea. Runs 3.1 to 6, which were performed in the cirrus, are shown in bold.

However, the only way of making simultaneous *in situ* microphysical and radiative sampling is using an aircraft platform. The inability to perform column measurements of cloud microphysics has an obvious effect on the extent to which a true measurement of the cloud conditions can be made. With this in mind, sensitivity studies have been performed to attempt to account for the extent to which the uncertainty of the boundary emissivity at the cirrus base and microphysics affects the modelled spectra. Even so, by looking for consistency in the MIR and FIR regions, it can be determined how far the scattering and absorption of FIR radiation is currently understood within the bounds of the experiment.

2. Description of measurements

On 11 February 2005, the FAAM aircraft flew over to the North Sea, where it performed several horizontal runs and vertical profiles in the cirrus, as shown by the position of the flight track plotted in Figure 1 and summarised in Table I. Starting at low level (0.8 km), the aircraft profiled up and performed two runs, forward and back along the same track (reciprocal runs) at 4.6 km, in a patch of low-level cloud present below the cirrus. Profiling up to the top of the cirrus, the FAAM aircraft then began a series of horizontal runs from the northeast to the southwest at four levels in

Table I. The mean altitude, temperature and pressure measured by aircraft instrumentation on each run during the flight of 11 February 2005. Observations recorded by the mission scientist are summarised.

Run/profile	Altitude (km)	Temperature (K)	Pressure (hPa)	Observations
R1	0.77	280	1016	Eastwards. Broken altostratus above.
P1				Ice crystals at 3.2 km and altostratus at 4.3 km.
R2.1–2.2	4.57	259	571	Run 2.1 southwesterly; Run 2.2 northeasterly. In cloud.
P2				Descent down to runs 2.1 and 2.2.
R3.1–3.2	10.03	217	262	Run 3.1 northeasterly; Run 3.2 southwesterly. Reciprocal runs in cirrus tops. Relatively clear at southwest end of runs.
P3				Profile up to follow leading edge of cirrus.
R4	9.46	222	287	Northeasterly run in clear skies, entering cirrus in second half which thickened.
P4				Profile down in relatively clear sky.
R5	8.85	227	314	Southwesterly run finishing outside cirrus.
P5				Profile down in cirrus.
R6	8.26	233	344	Relatively clear patch below cirrus with stratocumulus below.
P6				Profile down in relatively clear sky.
R7	5.54	255	506	Northeasterly. In nominal tops of altostratus. Run started in cloud, which cleared to leave cirrus above.

the cloud (reciprocal runs 3.1 and 3.2 at 10.0 km, run 4 at 9.5 km, run 5 at 8.9 km and run 6 at 8.3 km, shown in bold in Figure 1), finishing in the nominal cirrus base at run 6 (8.3 km). The cloud visibly thinned in a southwesterly direction, and this was confirmed by the microphysical data and radiative measurements. The time taken to move from the top of the cloud to the nominal base was 76 min, and careful processing of the auxiliary measurements was required to acquire the cloud properties most representative of the scenes viewed by the radiometers during flight for modelling purposes. Despite these difficulties involved with sampling the cloud, this flight proved a useful one to study the radiative effect of cirrus in the MIR and FIR due to the presence of both TAFTS and ARIES on board the FAAM aircraft, and the varying optical thickness of cirrus conditions encountered.
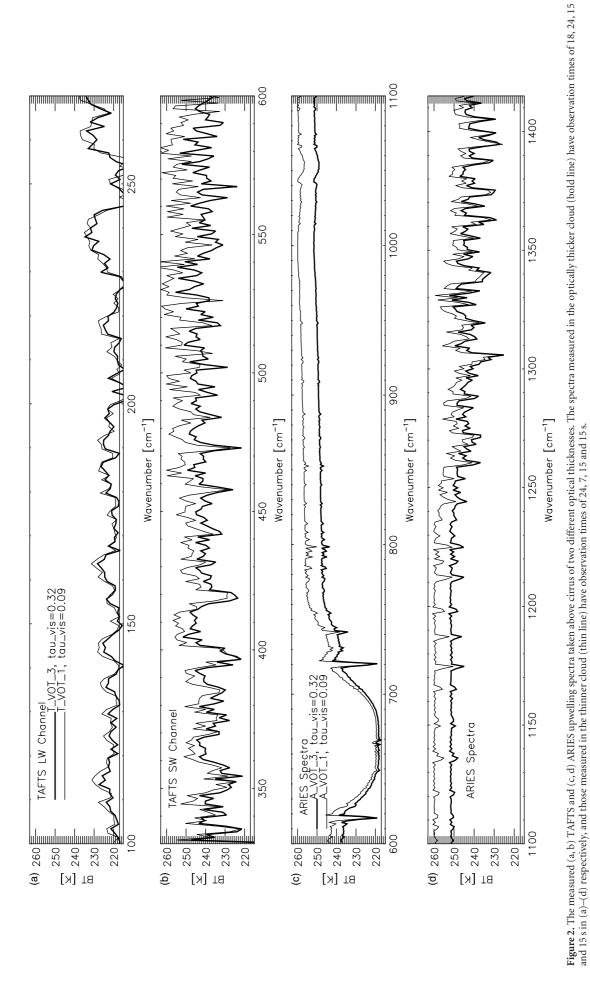
2.1. Radiative measurements

Together, TAFTS and ARIES are capable of measuring radiances between 100 and 3000 cm^{-1}. TAFTS is a polarising Martin–Puplett type interferometer that measures radiation at a maximum spectral resolution of 0.12 cm^{-1} in two channels, long wave (LW) 100–270 cm^{-1} and short wave (SW) 330–600 cm^{-1}. ARIES measures at a maximum spectral resolution of 1 cm^{-1} between 550 and 3000 cm^{-1} in two channels, although only the longer-wavelength channel has been used in this study as our interest is in the relatively long wavelength radiative transfer in cirrus. For consistency, and to improve the signal-to-noise ratio, TAFTS spectral resolution has been reduced to that of ARIES.

Radiance spectra were selected primarily for optimal coincidence of TAFTS and ARIES views. Both instruments can view zenith and nadir sky views, although, as TAFTS and ARIES operate independently and both require views

of internal calibration targets in-flight, their views do not always coincide. Also, a reduced number of spectra were available from TAFTS due to the elimination during analysis of raw spectra affected by sampling ghosts (Davis *et al.*, 2001) explained later in this section. Ultimately, two sets of near-coincident TAFTS and ARIES spectra were selected for this analysis study and calibrated. Both spectra were measured at the top of the cloud on runs 3.1 and 3.2 looking down, under condition of two different cirrus optical thicknesses.

Both spectra in Figure 2 are shown at 1 cm^{-1} resolution. The TAFTS co-added spectra are labelled T_VOT_3 and T_VOT_1, measured when the cirrus visible optical thickness was around 0.3 and 0.1 respectively. The values of the optical thickness were derived from the PSDs that provided a fit to the ARIES infrared window region (section 3.2).

Spectrum T_VOT_3 contains twelve (LW channel) and nine (SW channel) raw co-added spectra taken between 1334:34 UTC and 1335:12 UTC, and consists of 24 s (LW channel) and 18 s (SW channel) of observation time. The total times over which the individual spectra were taken for these sets of co-added spectra are 72 s for both the LW and SW channels. The corresponding ARIES co-added spectrum, hereafter referred to as A_VOT_3, is composed of twelve spectra, each produced from co-adds of ten scans. The twelve spectra were recorded between 1334:37 and 1334:59 UTC. The resulting co-addition represents 15 s of observations.

TAFTS spectrum T_VOT_1 contains twelve (LW channel) and seven (SW channel) raw co-added spectra taken between 1318:14 UTC and 1318:45 UTC, giving 24 s (LW channel) and 14 s (SW channel) of observation time. The total integration times for these spectra are 31 s for both the LW and SW channels. The ARIES spectrum, hereafter

Figure 2. The measured (a, b) TAFTS and (c, d) ARIES upwelling spectra taken above cirrus of two different optical thicknesses. The spectra measured in the optically thicker cloud (bold line) have observation times of 18, 24, 15 and 15 s in (a)–(d) respectively, and those measured in the thinner cloud (thin line) have observation times of 24, 7, 15 and 15 s.

referred to as A_VOT_1, is composed of twelve spectra, each produced from co-adds of ten scans. The resulting co-addition is 20 s of observations taken between 1318:25 and 1318:59.

The calibration of TAFTS spectra was performed using in-flight views of four calibration targets, two held at temperatures of ≈ 275 K and two at temperatures of ≈ 310 K, with two black bodies at each temperature in the upwelling and downwelling arms of the instrument. These calibration scans determine the instrument response function and instrument self-emission term, so that a sky-view raw spectrum can be calibrated. TAFTS has two complementary outputs and so, to improve the signal-to-noise ratio, complementary LW channel measured interferograms are combined. For SW spectra, only one of the outputs is used since one of the two SW channels, through analysis of laboratory data, is known to be affected by instrumental effects leading to poor quality calibration. Therefore, higher noise levels are present in the SW TAFTS spectra than in the LW.

The principal source of uncertainty in TAFTS spectra is due to detector noise. This random error can be measured in flight using the imaginary part of the raw spectrum, as shown in Green (2003), and it is this which dominates the brightness temperature uncertainty for flight spectra unaffected by vibrations. This error is dependent on the number of spectra used in a co-added spectrum. The mean band brightness temperature uncertainty (random error) for TAFTS LW channel is 1.6 K and 1.8 K for spectra T_VOT_1 and T_VOT_3 respectively. For the TAFTS SW channel, the mean band brightness temperature uncertainty is 4.1 K and 3.8 K for spectra T_VOT_1 and T_VOT_3 respectively.

The random error associated with a set of ten co-added ARIES spectra is less than 0.1 K between 750 and 1250cm^{-1} (Wilson *et al*, 1999). Although co-adding more spectra together, as performed for this work, would normally decrease the uncertainty, when on a fast-moving aircraft the potential scene variation would affect the precision of the co-added radiance spectra measured. Therefore in this work the brightness temperature uncertainty associated with spectra A_VOT_3 and A_VOT_1 are the standard deviations of the individual ARIES spectra that compose the final co-addition. Over the infrared window region (750–1250cm^{-1}), the mean brightness temperature uncertainty is 1.2 K and 0.8 K and for the region 1250–1415cm^{-1} it is 1.9 K and 1.0 K for spectra A_VOT_1 and A_VOT_3 respectively. The same method of determining brightness temperature uncertainty due to scene variation was performed for the TAFTS spectra, where the standard deviation of individually calibrated spectra which made up each final co-addition was calculated. For spectra T_VOT_1 and T_VOT_3, the mean band brightness temperature uncertainty is 2.4 K and 2.6 K respectively for the LW channel and 4.7 K and 4.3 K respectively for the SW channel. These values also include the random noise, previously discussed. It is this uncertainty that is plotted alongside the calibrated TAFTS spectra.

In the flight environment, vibrations of instrument can also affect the quality of the spectra, leading to sampling ghosts. In TAFTS, the interferograms are initially sampled at equal temporal intervals and later re-sampled spatially by use of a metrology laser and the application of the Brault sampling technique (Brault, 1996) to account for variations in the optical path difference (OPD) due to, for

example, instrument vibrations. However, the FIR beam and metrology laser beam travel through different areas of the TAFTS interferometer beamsplitter, and vibrations can differ in amplitude and phase, so each beam experiences different OPDs which cannot be corrected with the Brault method. A sampling error of frequency ε develops, resulting in every spectral line, including the continuum, having two associated copies, or 'ghosts', positioned at $\pm\varepsilon$ from the parent line. The amplitude of each ghost is proportional to both the amplitude of the sampling error and the parent line wavenumber, and hence the TAFTS SW channel, having higher wavenumbers, is affected more that the LW channel. If the frequency of the periodic sampling error is less than the bandwidth associated with the free spectral range, then the 'continuum ghost' will have some overlap with the main spectral region and, in this case, the beamsplitter vibration is uniform in the time domain. When the interferogram is re-sampled to a spatial domain, the vibration frequency will be smeared out, proportionally to the variations in the mirror velocity. With a slow variation of relative phase, the signature of these vibrations may be expected to be distributed throughout the spectrum, resulting simply in an increased noise level (Thorne *et al*, 1999). This is true if the interference at all points of the interferogram is similar in modulation magnitude. In the case of a continuum spectrum, the coherence near zero path difference is at a maximum, and the quasi-constant phase over the zero path difference means the associated continuum ghosts (although spread by the scan speed variation) will appear as distinct features (shifted copies of the original spectrum), adding to and distorting the continuum level of the spectrum of interest. This distortion is seen in TAFTS flight data exhibiting a scan-to-scan variation which is attributed to the relative phase between the vibration and interferogram sample at zero path difference of each scan. For example, if the phase difference between the sampling error and sampling frequency is $\pi/2$, then the copy of the spectrum shifted to lower frequencies would be negative and the copy shifted to higher frequencies would be positive, hence showing a 'tilt' in the ghosted spectrum. The magnitude of the ghost ultimately depends on the relative phase of the vibration for any individual scans, and the maximum ghost magnitude is calculated to be about 10% of the spectrum from a signal at 300cm^{-1}. The ghosting is not removed in the calibration process as the ghosts in the calibration views may not be the same as those in the view spectra due to variations in the beamsplitter vibrations and the relative spectral power distribution of the calibration sources differing from the scene. When processing the TAFTS raw data, the significantly ghosted spectra are simply excluded by rejecting spectra with any signal outside of the limits of the detector and associated filters. However, even though this rejection process is performed, ghosting in the spectra may still be present and must be considered in the analysis of measured and simulated spectra.

In Figure 2(a), spectra measured in TAFTS LW channel (100–270cm^{-1}) are plotted. In this wavenumber region, there are strong water vapour absorption lines, where the spectra saturate at the ambient temperature of 217 K, as measured by an aircraft temperature sensor. In between these strong absorption lines are microwindow regions, where there is little absorption from water vapour so that radiation from lower altitudes in the atmosphere

and the surface is able to reach the observation level. The two TAFTS LW spectra measured over the two cirrus conditions show similar brightness temperatures, within the mean brightness temperature uncertainty over that wavenumber band (2.5 K). This may be because the spectra were only sensitive to the upper layers of the cirrus where the cloud optical depth did not vary very much along the run. At higher wavenumbers in the LW channel spectra, there are several points where the brightness temperature dips below the ambient temperature, for example between 200 and 205 cm^{-1} and at 228 cm^{-1}. These are likely to be due to strong water vapour absorption lines which saturate at the higher temperatures in the fore optics section of TAFTS and can cause problems in the calibration. Electrical pickup was present in the interferograms causing an erroneous signal in the spectra around 245–255 cm^{-1} and hence the strong absorption lines in the calibrated spectra sit below the ambient temperature.

In Figure 2(b), which shows TAFTS SW channel (330–600 cm^{-1}) spectra, there are similar microwindow regions to those observed in the LW channel, however since the atmosphere is more transparent at these higher wavenumbers a higher brightness temperature is observed. The upwelling spectrum measured over optically thinner cirrus has much higher brightness temperatures in the microwindows (by around 10 K) due to the increase in transparency of the cloud, so that radiation from the warmer cloud and atmospheric layers below is detected.

Figure 2(c) shows the measured ARIES upwelling spectra A_VOT_3 and A_VOT_1 between 600 and 1100 cm^{-1}. The carbon dioxide absorption band is observed centred at 667 cm^{-1}, where both the spectra saturate at ambient temperature. There is a rapid increase in brightness temperature between the carbon dioxide absorption band centre and 760 cm^{-1} where the atmospheric weighting functions change significantly and hence this region is often used for cloud height determination (Holz *et al.*, 2006). In the infrared window region from 750 to 1250 cm^{-1} there is little absorption by water vapour, but the brightness temperature remains relatively low in both cases due to the cloud cover. There is a gradient to the brightness temperature in both spectra between 750 and 1100 cm^{-1}, indicative of the presence of optically thin cloud. The difference in brightness temperature between spectra A_VOT_3 and A_VOT_1 is again up to 10 K.

In Figure 2(d), where the ARIES spectra continue up to 1415 cm^{-1}, there is increased water vapour absorption occurring beyond the window region. The methane absorption band, centred at 1306 cm^{-1} is apparent, where the two spectra converge.

Information on the optical thickness of the underlying cirrus can be gained by looking at the variation in brightness temperature from all the ARIES spectra measured during the highest-altitude runs. When cirrus is present, the brightness temperature of the underlying scene will be lower than for a clear scene. In Figure 3, the geographical locations of runs 3.1 and 3.2 are plotted as a function of latitude and longitude, as well as the positions of the measurements of TAFTS spectra T_VOT_3 and T_VOT_1 for reference. Also shown by a marker are the locations at which individual ARIES upwelling spectra are measured. The marker also indicates by its size the mean brightness temperature between 999
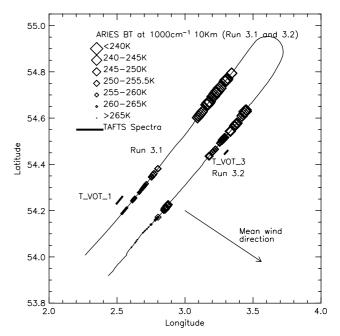

Figure 3. The tracks of runs 3.1 and 3.2, with the locations of ARIES upwelling spectra measured along the runs marked with the mean brightness temperatures measured between 999 and 1001 cm^{-1}, with values indicated by the symbol sizes shown in the key. Positions of the two sets of co-added upwelling TAFTS spectra are indicated by bold black lines offset from the run.

and 1001 cm^{-1} for each spectrum. The wavenumber region 999–1001 cm^{-1}, selected because of its low water vapour absorption, gives an indication of the variation of the optical thickness of the cirrus. The brightness temperature measured at this wavenumber interval increases towards the southwest by up to 25 K, in agreement with visual observations that the cirrus was becoming optically thinner in this direction.

2.2. Description of auxiliary measurements

Cloud microphysical measurements were recorded throughout the flight, along with pressure, temperature and dew point temperature by core instrumentation on board the FAAM aircraft. These were important in allowing the simulation of spectra for comparison with observations. The instruments available for sampling ice particles were a 2-dimensional cloud (2DC) and a 2-dimensional precipitation (2DP) probe (Knollenberg, 1976). These measure particle size and concentration. Automatic processing of the ice particle measurements also produced estimates of ice water content (IWC).

It was important to ensure that the microphysics input to the model used to simulate the spectra was as representative as possible of the scene viewed by TAFTS and ARIES when at the top of the cloud taking radiance measurements. However, the horizontal runs in the cirrus were not precisely vertically stacked and the cloud field was advecting and changing form. Hence, the column of cloud and atmosphere directly below the two sets of radiative measurements were not perfectly aligned. The area over which the aircraft performed all runs and profiles was 380 by 280 km, and the separation between runs within cirrus can be seen in Figure 1. For modelling purposes, it was assumed that the cloud varied only along the length of the runs, perpendicular to the direction of the wind and the microphysical measurements were then averaged over 20 km sections. The potential

problem of sampling a moving cloud from a fast-moving aircraft was dealt with by advection of the measurements in space and time using wind velocity data from the aircraft. By doing so, the position of each air 'packet' when the spectral measurements were taken at the top of the cloud was estimated, to attempt to find the PSDs most representative of the column of cloud below the two sets of radiative measurements.

The two cloud probes complemented each other, with the 2DC probe measuring ice between 25 and 800 μm at 25 μm resolution, and the 2DP cloud probe measuring 200–6400 μm at 200 μm resolution; however, measurements of ice particles smaller than 25 μm, normally performed with the Small Ice Detector (SID), were not possible due to an electrical fault. The PSDs measured on each run and each of the two sections of cloud are shown in Figure 4. In the cirrus layer itself, all the ice particle sizes fell within the measurement range of the 2DC probe (25–800 μm) and so only the 2DC data is used for information on the cloud microphysics. The width of the bins are therefore 25 μm to represent the resolution of the 2DC probe, and the error bars represent one standard deviation of all the PSDs measured in each section. These errors are often large, but there is still a clear distinction in ice number density between the PSDs from each end of the cloud in the centre layers where most of the ice is contained. The figure also shows there may be a large number of small ice particles missing, since each PSD peaks in the lowest size bin. Ice crystals smaller than 100 μm measured by the 2DC probe are used in this work even though these small particles are often disregarded due to reported problems with the 2DC probe sizing them (Field *et al.*, 2005). The 2DC measurements of ice smaller than 100 μm are considered the best estimate available of the PSD at small sizes, however the effects of potential errors in counting these small crystals are tested in section 5.4.

The IWC is calculated automatically from the 2DC measurements of PSD. The IWC used in this work is found using a mass to area relationship given in Eq. (1), which uses the density of water ρ, the number of particles n in bin i, and the diameter of a water droplet of equivalent mass of the particle D_{eq}. Equation (2) shows that D_{eq} is dependent on the particle area A and two constants, a and b, which depend on the crystal habit (Cunningham, 1978).

$$IWC = \frac{\pi \rho}{6} \sum n_i D_{eq}^3, \qquad (1)$$

$$D_{eq} = aA^b. \qquad (2)$$

The mean values of the IWC in the two sections that encompassed the measured spectra are plotted in Figure 5. These also illustrate the marked differences in the cloud conditions between the two ends of the cloud. The middle layers showed the most variation in ice content, and these were also at the most coarse vertical resolution.
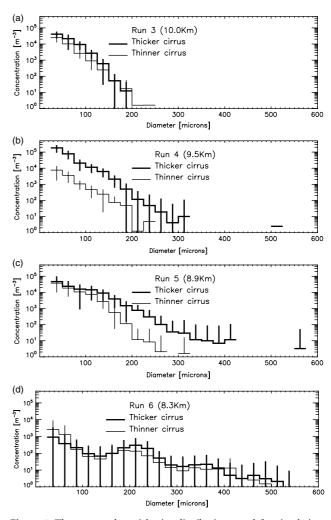

Figure 4. The measured particle size distributions used for simulations of spectra measured above optically thin and thick cirrus. The error bars represent the standard deviations of the concentrations measured in each size bin.
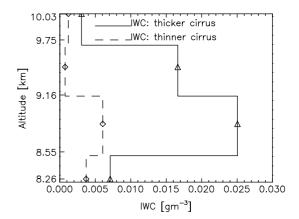

Figure 5. The ice water content derived from the 2D cloud probe, as a function of altitude, for the four layers defined within the cirrus, for both the optically thin and thicker cloud. The altitude at which the ice water content was measured is shown by the diamond and triangle markers.

3. Modelling TAFTS and ARIES spectra

Modelling the radiance spectra measured by the two spectrometers was performed using a combination of the Line by Line Radiative Transfer Model (LBLRTM; Clough *et al.*, 2005) and the Line by Line Discrete Ordinates Radiative Transfer Model (LBLDIS; Turner, 2005).

LBLRTM was used to calculate the radiance at every spectral line within the desired wavenumber range and spectral resolution, from inputs of measured temperature and relative humidity as a function of pressure. Information about the temperature T, was taken directly from the aircraft Rosemount temperature sensor. The humidity

profile was derived from measurements of dew (or frost) point temperature T_d from the General Eastern Hygrometer on board the FAAM aircraft. The dew point measurements were converted into a relative humidity (RH) using Eq. (3) (Seinfeld and Pandis, 1998):

$$RH = 100 \times \exp\left\{5417.1\frac{(T_d - T)}{T^2}\right\}. \qquad (3)$$

Information on concentrations of other atmospheric gases active in the region of interest (carbon dioxide, ozone, methane) was based on the standard US 1976 atmosphere (NOAA *et al.*, 1976), which was adequate for this work since ozone has only weak absorption lines and carbon dioxide and methane have no absorption lines in the FIR. LBLRTM uses the HITRAN line database (Rothman *et al.*, 2005) and has the advantage of being regularly updated with new water vapour continuum models. The version of LBLRTM used in this work was version 9.4 and uses the MT CKD 1.2 water vapour continuum (Clough *et al.*, 2005). LBLRTM also has the advantage of being operated complementary to LBLDIS.

The model used to calculate the scattering and absorption of radiation in the cloud, LBLDIS, uses the Discrete Ordinates Radiative Transfer Method, DISORT, to calculate the radiative transfer in a vertically inhomogeneous atmosphere (Stamnes *et al.*, 1988). The cloud is split into a number of layers and LBLDIS reads in optical depths and temperature profiles produced by LBLRTM of the same cloud-free atmospheric layers. Each cloud layer is then assigned a bulk scattering albedo, asymmetry factor and cloud optical thickness. These bulk cloud properties describing the scattering and absorption properties of the cloud are derived from integrating single scattering properties over the measured PSDs and layer thickness (Baran, 2005). In this case, the single scattering properties of aggregate and hexagonal column ice crystals were used (Baran and Francis, 2004). Using additional information on the lower boundary temperature and emissivity, the radiance at any given layer and resolution can be calculated with LBLDIS. Further details of how the cirrus and lower atmosphere were characterised in the model are discussed in the next two sections.

The resolution of the model output is set to $1\,\text{cm}^{-1}$ in agreement with that of the ARIES spectra and reduced-resolution TAFTS spectra. For this work it has not been necessary to match the apodisation used for TAFTS and ARIES spectra of each instrument in the model as the broadband cirrus effects are more important than line shapes.

3.1. *Characterising the atmosphere below the cirrus*

The characterisation of the atmospheric conditions below the cirrus layer is complicated by the presence of lower cloud layers. Due to the large spatial scales involved, it is very difficult to be able to accurately represent the microphysics of any underlying cloud present when radiative measurements were taken at the top of the cirrus. For simplicity in modelling, the base of the cirrus layer at 8.3 km has been taken as the lower boundary of the model, and it is constrained using actual radiative measurements from TAFTS and ARIES rather than directly using measured PSDs and atmospheric properties between the sea surface

and the base of the cirrus. The lower boundary in the model is then simply formed from the radiance measurements on run 6 at 8.3 km rather than using the temperature and emissivity of the surface. The base of the cirrus is defined as being at 8.3 km altitude simply because this was the altitude of the aircraft run (run 6) most closely associated with the observed base of the cirrus. The vibration problem associated with TAFTS, discussed in section 2.1, has meant that the number of available good quality and coincident ARIES and TAFTS upwelling spectra measured at the cirrus base is limited. There was only one occurrence of vibration-free TAFTS and ARIES spectra that were coincident along run 6. It is important to ensure that the boundary spectra are coincident so as to maintain consistency in the simulations across the infrared. Any uncertainty in the simulated spectra due to the boundary conditions is tested in section 5.2.

The TAFTS and ARIES spectra used to produce the boundary conditions at 8.3 km are plotted in Figure 6 with a simulated spectrum produced using dropsonde measurements of RH and temperature, assuming clear-sky conditions. The TAFTS LW spectra shown in Figure 6(a) are in close agreement with the clear-sky model, showing little sensitivity to the cloud present below the cirrus. In Figure 6(b), the TAFTS SW measurements agree with the clear-sky simulation at wavenumbers less than $360\,\text{cm}^{-1}$, but then show a lower brightness temperature due to the presence of cloud. The ARIES spectra plotted in Figures 6(c) and (d) show a significant difference ($>20\,\text{K}$) from the clear-sky modelled spectra up to $1360\,\text{cm}^{-1}$, due to the transparency of the atmosphere at these high wavenumbers.

3.2. *Characterising the cloud*

Using the measurements of the PSD, cloud geometric thickness and knowledge of the theoretical single scattering properties of a particular shape of ice crystal, the bulk scattering and absorption properties of a cloud can be calculated. For this work, the majority of ice was classified by the 2DC probe as 'small ice', meaning it was below the minimum threshold where a specific crystal habit could be assigned to it. Initially an ice aggregate shape was used in the models (Baran and Francis, 2004) and the sensitivity of modelled spectra to a different crystal shape are later tested in section 5.3.

The measured PSDs shown in Figure 4 were not used directly in the modelling since they are missing vital information on ice particles smaller than 25 μm. In addition, the coarse vertical resolution and imperfect vertical stacking of the runs has resulted in the measured PSDs being adjusted in order to provide a model that shows agreement in the relatively well-understood infrared window region of the ARIES spectra. By fitting the microphysics to the window regions of both spectra, it has been possible to look for consistency in modelling the FIR and MIR.

Adjustment of the measured PSDs, which were taken to be the initial best estimates, was based upon sensitivity of the modelled spectra to both crystal size and total IWC. The brightness temperature difference between 790 and $960\,\text{cm}^{-1}$, which was 2.9 K for both the optically thick and thin cirrus, was used as a measure of the sensitivity of the mean particle diameter, with a larger difference signifying the presence of smaller ice crystals (Huang
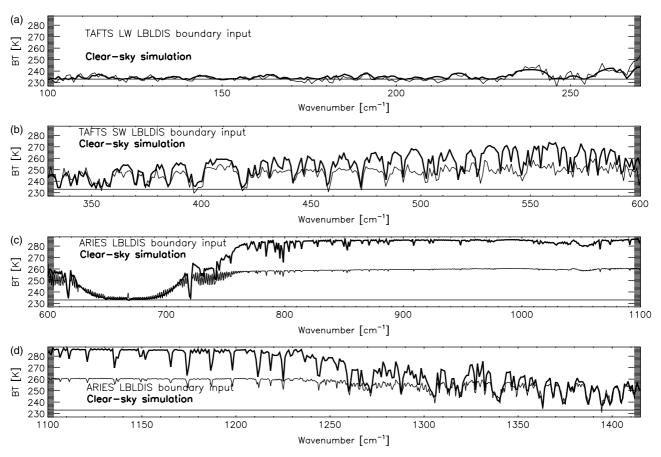
Figure 6. Spectra measured on run 6 at 8.3 km for (a) the TAFTS LW channel, (b) the TAFTS SW channel, (c) the ARIES window infrared region, and (d) the ARIES MIR region. The bold curves show the corresponding clear-sky simulations.

et al., 2004). Sensitivity to total ice is observed in the 1100 to 1250 cm^{-1} region, with an optically thicker cloud giving lower brightness temperatures here. Adjustments to the mean ice diameter and total ice content were performed iteratively. Using the original unadjusted PSDs, the brightness temperature difference between 790 and 960 cm^{-1} in the simulated spectra was 2.6 K and 2.0 K for the optically thicker and thinner cloud respectively. The mean difference in measured and modelled spectra over the region of 1100 to 1250 cm^{-1} was 5.2 K and 1.5 K for the optically thicker and thinner cloud respectively, demonstrating the need to make adjustments to the measured PSDs.

In the PSDs, ice crystals smaller than 25 μm were added in bins of 5 μm width, to simulate measurements that would have been taken with the SID. In order to achieve a realistic proportion of ice in each of the five size bins, a parametrisation relating the PSD to temperature and IWC was used (Field *et al.*, 2005). The measured temperature and IWC from the aircraft were used in the parametrisation as an initial starting point, and the IWC increased until the brightness temperature difference between 790 and 960 cm^{-1} agreed with that of the measured ARIES spectra. Then, the amount of ice in each PSD between both 0–25 μm and 25–800 μm was scaled by a constant factor so that the mean brightness temperature between 1100 and 1250 cm^{-1} agreed with the measured ARIES spectra. This was repeated in an iterative sense until the brightness temperature difference between 790 and 960 cm^{-1} agreed with that observed in the ARIES measurements, 2.9 K, for both the optically thicker and thinner sections of the cirrus

respectively. Agreement of the mean brightness temperature over the 1100 to 1250 cm^{-1} region with the measured ARIES spectra was achieved within ARIES brightness temperature uncertainty (1 K).

Differences between measured and modelled ARIES spectra are shown in Figure 7(a) and (c) for A_VOT_3 and A_VOT_1 respectively. The differences are shown at a resolution of 3.8 cm^{-1}, lower than the original resolution of the ARIES spectrum (1 cm^{-1}), to see more easily the broadband difference in the signal due to the presence of cirrus. The respective ARIES brightness temperature uncertainties are the standard deviations of all the individual ARIES spectra that go into the final spectral co-addition and are shown in Figure 7(b) and (d). The plots show that the differences between measured and modelled spectra across the window wavenumber range are within the 1 K uncertainty of the instrument: in both spectra the largest discrepancy of 0.7 K occurs around 1000 and 1050 cm^{-1}. These wavenumbers are where ozone absorbs and clearly the model does not have the correct ozone profile, as might be expected since a standard 1976 atmosphere was used. Such differences are not problematic for this study since the regions of interest, which are outside the ozone region, agree well. The brightness temperature difference between 790 and 960 cm^{-1} in particular agrees with the measurements within ARIES uncertainty.

The modified PSDs that produced the fit to the window region and were subsequently used to simulate the FIR spectra are plotted in Figure 8 together with the original measured PSDs, again plotted with error bars signifying the standard deviation of the PSD measurements in that section.
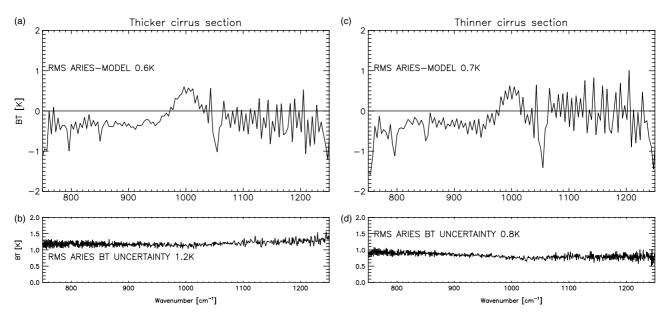
Figure 7. Differences (K) from the modelled spectra for ARIES spectra (a) A_VOT_3 and (c) A_VOT_1. (b) and (d) show the corresponding ARIES brightness temperature uncertainties.
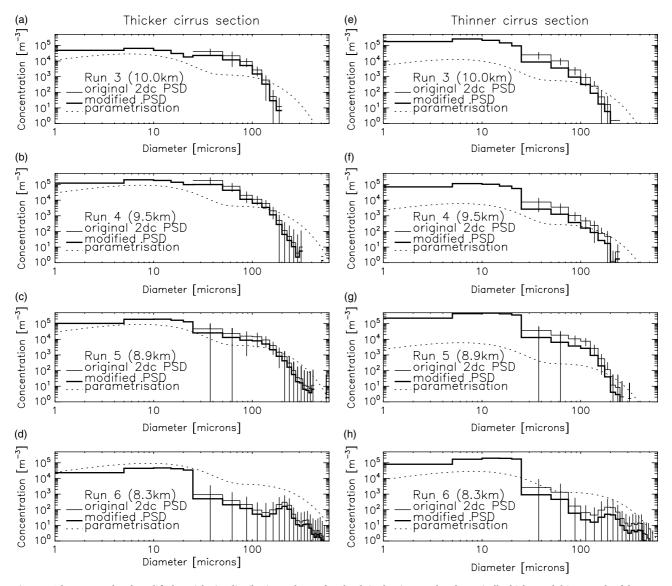

Figure 8. The measured and modified particle size distributions taken at four levels in the cirrus and at the optically thicker and thinner ends of the run. (a)–(d) show the optically thicker cirrus and (e)–(h) show the optically thinner cirrus, at levels 10.0, 9.5, 8.9 and 8.3 km, respectively. Also shown are the PSDs calculated from the Field *et al.* (2005) parametrisation using measurements of IWC and temperature measured on the FAAM aircraft.

Also plotted for comparison are the PSDs derived from the Field *et al.* (2005) parametrisation, using the original measured IWC and temperature as input. The modified PSDs were found to agree with the initial measurements within the uncertainties in most of the size bins. Many of the modified PSDs peak within the added small ice range, and some show bimodality (e.g. Figures 8(d) and (h)), which is a feature sometimes observed in cirrus (Field, 2000). The parametrised PSDs, when compared to the fitted 2DC PSD measurements, show a lack of small ice in seven out of the eight plots, however no attempt was made to adjust the IWC input to the parametrisation to achieve a fit to the window region.

The mean effective diameter of the ice in each section and layer has been calculated using Eq. (4), where $V(D_m)$, $<A(D_m)>$ and $n(D_m)$ are the volume, average cross-sectional area and number concentration of ice particles at each maximum dimension D_m respectively (Baran, 2005):

$$D_e = \frac{3}{2} \frac{\int V(D_m)\, n(D_m)\, dD_m}{\int <A(D_m)>\, n(D_m)\, dD_m}. \qquad (4)$$

The values of D_e were calculated to be 20, 23, 31 and 37 μm from the upper to lower layers for the optically thick section, and 22, 27, 30 and 71 μm for the optically thinner section, indicating little horizontal variation in ice particle size within the cloud. The visible optical thickness τ_{vis} has been found from the modified PSDs using Eq. (5):

$$\tau_{vis} = 2d \sum_i A_i n_i. \qquad (5)$$

The cloud layer thickness is d, the cross-sectional area A and concentration n are summed over size bins i. The optical thickness was calculated to be 0.3 in the thicker cloud and 0.1 in the thinner cloud.

4. Results of modelling across the infrared

4.1. Long-wave channel FIR

Figures 9(a) and (d) show the TAFTS LW channel spectra measured over optically thick and thin cloud respectively, together with the corresponding modelled spectra. The corresponding differences between model and measurements are shown in Figures 9(b) and (e), and the TAFTS brightness temperature uncertainty in Figures 9(c) and (f). In both cases, the simulated spectra do not agree with the measured TAFTS spectra within the instrument uncertainty when averaged across the band, with the RMS difference between measurements and simulations being 2.8 K and 3.6 K for the optically thick and thin cases, compared with RMS brightness temperature uncertainties of 2.1 K and 2.8 K. In both spectra there are particular differences in the simulated and measured spectra in particular microwindows; for example at 137 and 145 cm^{-1} for the optically thick cirrus case in Figure 9(a) the simulated spectrum shows lower brightness temperatures than the measured spectra. For the optically thin case, microwindows at 137 and 145 cm^{-1} also show a lower brightness temperature than the TAFTS spectra, whereas at 192, 218 and 239 cm^{-1} the microwindows of the simulated spectrum are at higher brightness temperatures
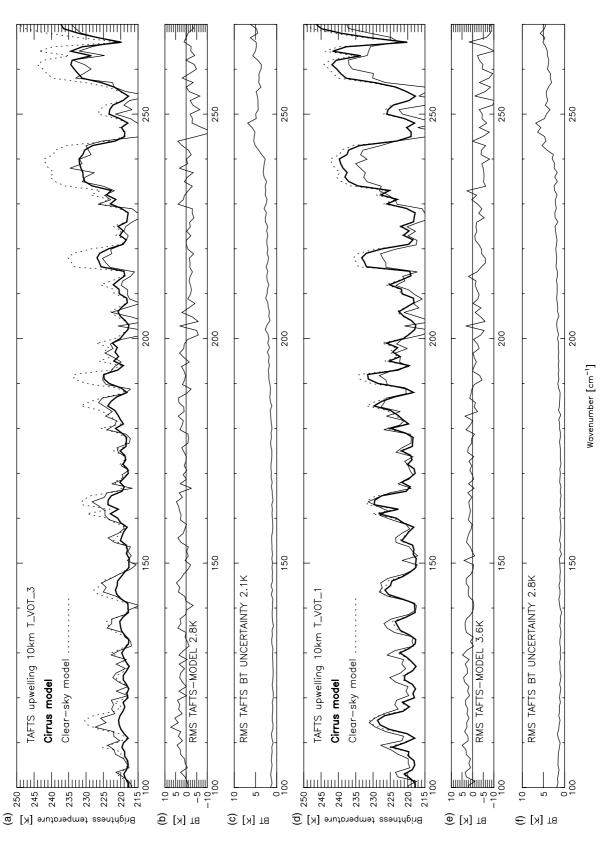
than the measurements. Between 160 and 190 cm^{-1} there is agreement within the instrument brightness temperature uncertainty. The measured TAFTS spectra, in particular in the optically thin case, show broadband differences that are positive at low wavenumbers and go negative at higher wavenumbers, potentially indicative of ghosting effects as discussed previously. Also plotted in Figures 9(a) and (d) with a dotted line is a simulation of the brightness temperature measured if no cirrus were present. This gives an indication of the absolute effect of the cloud on the radiation measured at 10 km. For the higher optical thickness case in Figure 9(a), there is a significant reduction in brightness temperature due to the cirrus cover, and some microwindows show up to 10 K difference between the measured TAFTS spectra and clear-sky simulation. In Figure 9(d), the cirrus does not seem to have much impact on the outgoing radiance. It is not until higher wavenumbers (192 cm^{-1} and beyond) that measurable differences between the clear-sky model and TAFTS measurements are evident. It is expected that for this case in particular, the RH profile will have a significant effect on the simulated spectra, and this is later tested in section 5.1.

4.2. Short-wave channel FIR

Figures 10(a) and (d) show the TAFTS SW channel spectra measured over optically thick and thin cloud respectively. The differences between model and measurements are shown in Figures 10(b) and (e), and the TAFTS brightness temperature uncertainty in Figures 10(c) and (f). The simulated spectrum does not agree with the observed TAFTS spectrum for the optically thick cloud shown in Figure 10(a) within the level of the TAFTS brightness temperature uncertainty of 4.3 K as the RMS difference averaged across the band is 5.5 K. The model consistently produces brightness temperatures in the microwindows that are lower than the measured spectra and it is not until around 550 cm^{-1} that the simulation and measurements converge. There is also disagreement between modelled and measured spectra in the presence of optically thin cloud, where the RMS difference averaged across the band is 7.1 K compared with the TAFTS brightness temperature uncertainty of 4.7 K. In this case the model also consistently gives lower brightness temperatures than is measured by TAFTS. A simulated clear-sky spectrum is plotted with the measured TAFTS spectra in Figures 10(a) and (d). In Figure 10(a), several microwindows show an increase in brightness temperature of up 10 K when there is no cloud present, however in Figure 10(d), the clear-sky model is almost coincident with the cirrus simulation. This shows the weak effect of the cloud in this case. Given the TAFTS brightness temperatures are greater than even the clear-sky model, this implies that the causes of the disagreement between model and measurements are not due to the cloud properties but due to either the boundary conditions or water vapour profile entered into the model. These uncertainties are both investigated in sections 5.1 and 5.2.
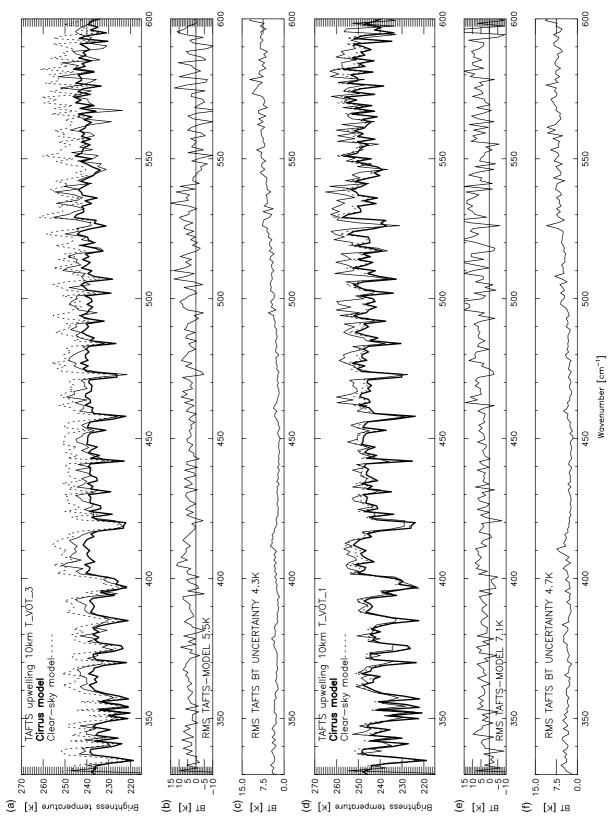
4.3. Mid-infrared

Figures 11(a) and (d) shows the ARIES spectra extending from the window region at 1250 to 1415 cm^{-1} measured over optically thick and thin cloud respectively. The differences
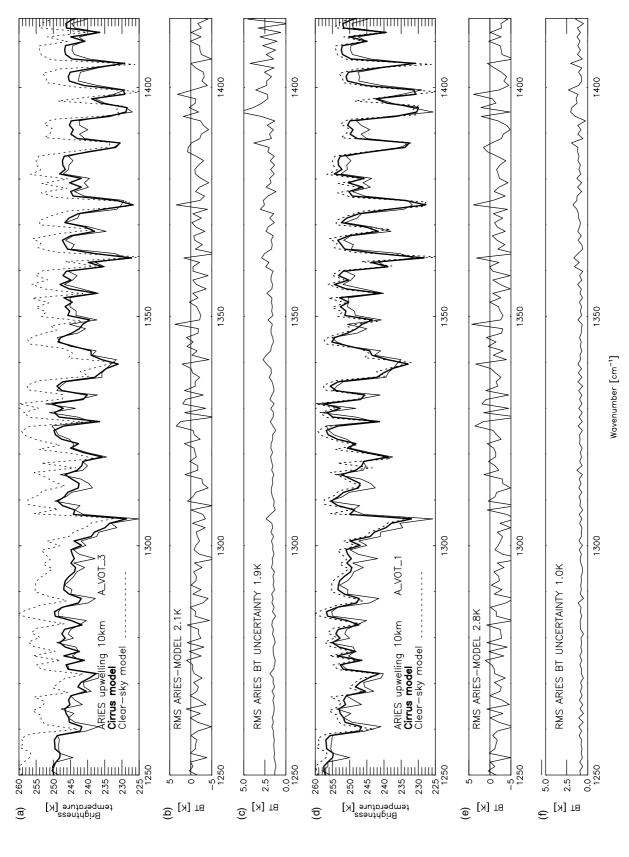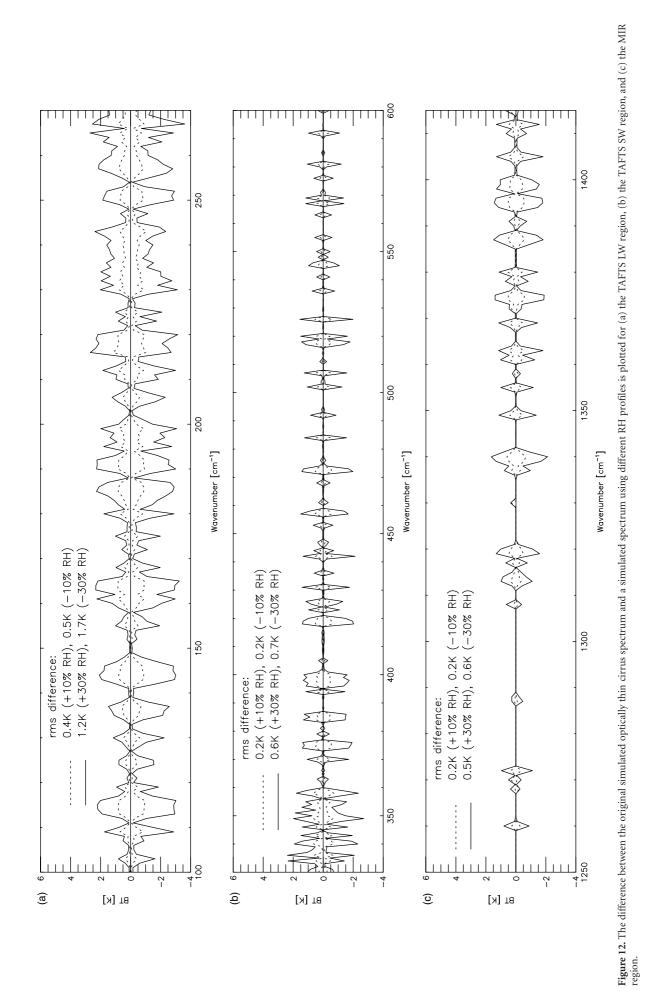
Figure 9. Measured TAFTS LW spectra (a) T_VOT_3 and (d) T_VOT_1 are shown together with modelled cirrus spectra, and (c) and (f) show the instrument brightness temperature uncertainty.

Figure 10. As Figure 9, but for the TAFTS SW spectra.

Figure 11. As Figure 9, but for the ARIES spectra.

Figure 12. The difference between the original simulated optically thin cirrus spectrum and a simulated spectrum using different RH profiles is plotted for (a) the TAFTS LW region, (b) the TAFTS SW region, and (c) the MIR region.

between model and measurements are shown in Figures 11(b) and (e), and the ARIES brightness temperature uncertainty in Figures 11(c) and (f). The optically thicker case in Figure 11(a) shows the model has a generally good agreement with the measured spectrum, with the RMS difference being 2.1 K compared to the mean instrument uncertainty of 1.9 K. The optically thinner case does not show such good agreement, with the RMS difference being 2.8 K compared to the mean instrument uncertainty of 1.0 K. In this case, the model is consistently giving higher brightness temperatures than the ARIES measurements, which is similar to that observed in the TAFTS SW channel, indicating both regions show similar inconsistencies in the model cloud. The clear-sky simulation also shown in Figures 11(a) and (d) indicates that the optically thicker cloud reduced the brightness temperature by up to 10 K from the measured ARIES spectrum, whereas the effect over the optically thinner cirrus is less than 2 K.

5. Sensitivity studies

It is instructive to investigate to what extent it is possible to reproduce the measured TAFTS and ARIES radiances, given the uncertainties present in the input to the model. Since the PSDs input to the model were adjusted to fit the window region, the largest uncertainties in the input to the model are thought to be the water vapour profile in the cloud layer, the boundary conditions at the base of the cirrus, ice crystal habit and errors in counting small ice particles. Here, the sensitivity of the modelled spectra to these uncertainties has been tested to understand how accurately the measured spectra can be simulated in such a case-study.

5.1. Sensitivity to relative humidity (RH) profile

The RH profile with respect to ice within the cirrus layer was measured by the General Eastern Hygrometer on the FAAM aircraft, as described in section 3. The typical instrument uncertainties in the measurement of RH are typically 5%, however the instantaneous column water vapour field below the measured spectra is not measured and so the RH within the model may not be representative of the true atmosphere.

The sensitivity of the simulated FIR and MIR spectra to the RH profile used in LBLRTM has been tested by simply adjusting the RH profile measured in the optically thin cloud section by 10% and 30% to produce both a wetter and drier atmosphere, although changes to all these RH profile measurements by the same percentage may result in some layers having unrealistic RH values. The magnitude of the RH at each of the four cirrus layer boundaries defined in the model were, for the optically thinner cirrus, 99.3%, 98.3%, 101.6%, 125.0% and 147.9% from the nominal base at 8.3 km to cloud top at 10.0 km. The optically thin cloud simulation will be more sensitive to the RH profile and so this is tested in preference to the optically thicker cirrus. The differences in brightness temperature between the original optically thin simulated spectra and the altered RH profile simulation are shown in Figure 12. Figures 12(a), (b) and (c) show these differences for the TAFTS LW spectral region, the TAFTS SW region and the ARIES MIR region respectively, along with the RMS differences between

original and altered simulated spectra when averaged across the band. The sensitivity to the water vapour in the window region (not shown) is less than 0.1 K in all cases and hence the RH profile would not affect the retrieved PSDs used in the model. There is greater sensitivity to the humidity profile in the TAFTS LW region than in the SW and MIR regions. The microwindows give brightness temperatures that are lower (higher) than the original simulation by up to around 3 K if the atmosphere is wetter (drier). The brightness temperature in the strong water vapour absorption lines is relatively insensitive to changes in the RH profile and still tends to saturate at the same temperature. The magnitude of the brightness temperature differences seen for the altered RH profiles are of the order of the mean TAFTS and model brightness temperature differences observed in the LW region, and so it is important to know the RH profile accurately.

The SW channel and the MIR regions shown in Figures 12(b) and (c) have mean band average brightness temperature differences of less than 0.7 K,–less than the instrument noise. The microwindow regions are unaffected by variations in RH and the greatest changes occur in the strong water vapour absorption line regions. This gives confidence that in the microwindows, at least for the FIR SW and MIR, the accuracy of the RH profile is not an important factor when simulating this cirrus case.

In this analysis, it has been assumed that the water vapour continuum used in the model, MT CKD 1.2, is correct. However, much work is ongoing to measure the continuum, in particular in the FIR where few measurements exist. If the continuum is incorrectly represented in the radiative transfer then this will add an additional uncertainty. In the MIR, there are more instruments able to measure radiation than in the FIR and therefore this spectral region is much better represented; for example, in clear sky the region 600–1400 cm^{-1} ARIES measurements have been found to agree with other instruments to better than 1 K (Newman *et al.*, 2009).

5.2. Sensitivity to boundary conditions

As described, measured coincident TAFTS and ARIES spectra at the base of the cirrus were used to define the lower boundary upwelling radiance. However, the presence, and geometric and optical thickness, of cloud below the cirrus was variable and with the limited number of coincident TAFTS and ARIES spectra available it is possible that unrepresentative boundary conditions were used. This changeable scene may result in modelled spectra not agreeing with measured spectra across the entire infrared region studied in this work. The boundary conditions used in the modelling were selected due to the coincidence of the TAFTS and ARIES spectra measured on run 6. It was thought preferable to use spectra that would give consistency across the entire infrared region and there was only one set of TAFTS and ARIES spectra suitable for this, as shown in Figure 6. Ideally, there would be several other sets of coincident TAFTS and ARIES spectra to run in the model to test the effect on the simulations at 10 km. However, as this is not possible, the sensitivity of the FIR is tested using clear-sky simulated spectra in the boundary.
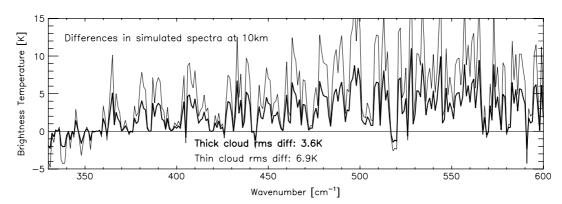
Figure 13. Brightness temperature differences between modelled optically thick and thin cloudy spectra for two different boundary inputs. One boundary used is based on TAFTS spectra measured below the cirrus, and the other boundary uses a clear-sky simulation.

TAFTS LW channel spectra have been found to be relatively insensitive to the boundary at the cirrus base, since the radiances measured at 8.3 km were similar to those produced from a clear-sky model. The atmosphere is much too opaque at the wavenumbers covered by the LW channel (100–270 cm^{-1}) to be sensitive to lower boundary conditions. The TAFTS SW channel spectra, however, may show significant sensitivity and this is now investigated. The clear-sky simulated SW spectrum plotted in Figure 6 has been used in the model, together with the modified PSDs that produced a fit to the window region in the optically thicker and thinner sections of the cloud. The differences between the original modelled spectra and the new modelled spectra produced with different boundary conditions are plotted in Figure 13. The mean band RMS differences are 3.6 K for the optically thicker case and 6.9 K for the thinner case. The two spectra are most similar at low wavenumbers less than 370 cm^{-1}, where the radiances are coming from higher altitudes in the atmosphere. The spectra are most sensitive in the microwindow regions, unlike the RH sensitivity. As expected, the differences for spectra simulated with different boundary conditions are greater for the optically thinner case because of the transparency of the cloud. For both cases the difference increases with wavenumber, indicative of the increasing transparency of the cloud and atmosphere with wavenumber. Although the differences for the optically thicker case are still within the noise level of the measured TAFTS spectra, the optically thinner case has differences that are comparable to the uncertainty of measured TAFTS spectra.

For both spectra, the differences between the simulated spectra with clear-sky boundary conditions and the original model are in the correct sense to improve the agreement between model and measurements, implying that less cloud cover was present below the cirrus when the upwelling radiative measurements were taken at 10 km than initially assumed. This analysis shows that a likely cause of the SW simulated spectra not agreeing with measured TAFTS spectra is due to incorrect boundary conditions. It also shows how vital it is that there is a well-sampled atmosphere below the cloud, as well as within the cloud, for such a study. It is far preferable to have clear sky beneath the cirrus layer rather than broken cloud for such a study.

5.3. Sensitivity to crystal shape

Some of the differences observed between model and measurements in TAFTS LW and SW channels may be due to an incorrect assumption about the ice crystal habit in the model, since several studies have shown that we would expect variations of radiance with crystal habit in the FIR (Yang *et al.*, 2003; Baran, 2005). To test the magnitude and type of effect for the particular cloud sampled, the aggregate crystal habit originally used in modelling was replaced by a hexagonal column (Baran and Francis, 2004). The same fitting method as used previously to determine the PSD with aggregates (subsection 3.2.1), including ice particles smaller than 25 μm and adjustment of the ice concentration in every bin, was carried out but for hexagonal columns. Such action will cause not only the crystal shape used in the model to be altered, but also the PSD shape, and so the effects of the PSD shape and crystal habit will be combined.

The differences between simulated spectra produced using aggregates and hexagonal columns are shown in Figure 14 (dotted line) for the entire infrared region. As the spectra have been modelled to produce a fit to the measured spectra in the window region, the differences between the aggregate model and hexagonal column model over this region in Figure 14(c) are small (<0.3 K), as would be expected. In the TAFTS LW channel in Figure 14(a), there are higher brightness temperatures in the hexagonal column model (up to 0.7 K) than with the aggregate model. This is due to the hexagonal columns having a higher D_e than aggregates for the crystal sizes encountered in this cloud and so are less absorbing than the aggregate crystal habits. In the SW channel in Figure 14(b), the largest differences are of the order of 0.5 K. The MIR shows little sensitivity to crystal shape, as the differences shown in Figure 14(d) are less than 0.3 K. Therefore, for this particular cloud, the effects due to crystal shape would not be detectable above the level of instrument noise and the disagreement between measured and modelled spectra is very likely not due to the use of inappropriate crystal shape in the cloud model.

To test if larger differences would be observed for an optically thicker cirrus case, the PSDs in both the aggregate cloud and hexagonal column cloud were increased by factors of 10 and 100, to increase the optical thickness from 0.32 to 3.2 and 32.0. The differences between the spectra modelled using aggregates and hexagonal columns for these two additional cases are also plotted in Figure 14. The differences between the aggregate and hexagonal column simulations in the FIR are now much larger: up to 3 K difference in the LW and 2 K in the SW for the ×100

Figure 14. The difference in the modelled spectra T_VOT_3 between using aggregates and using hexagonal columns, for cirrus with 100- and 10-fold increases (and also no change) in optical thickness for TAFTS (a) LW and (b) SW channel spectral regions. Equivalent data are shown for (c) the infrared window region and (d) the MIR 1250–1415 cm^{-1} region.

optically thicker simulated cloud, and up to 2 K and 1.5 K for the ×10 optically thicker cloud. Smaller differences (<0.5 K) are present in the 1070–1415 cm^{-1} region and in the window. This is consistent with the findings of Baran (2005). The shape of the differences in the FIR is related to the imaginary part of the refractive index of ice. It is clear that, the optically thicker the cloud under study is, the more important it is to get reliable information on the actual habit from which the cloud is composed. It would also be possible to use TAFTS FIR measurements to get information on the crystal habit, more so than the MIR. It is also difficult here to separate out the effects of the PSD shape from the crystal habit since different PSD shapes were used for both tests of crystal habits.

Intrinsic to the calculation of ice crystal scattering properties is the ice refractive index. In this work, the refractive index of Warren (1984) is used throughout, however an updated database of values has been published by Warren and Brandt (2008) which has not yet been implemented into any single scattering property databases. Any changes in the value of the refractive index may potentially impact the simulated radiances in this work.

The Warren (1984) and Warren and Brandt (2008) real and imaginary refractive indices are plotted in Figures 15(a) and (b). The most significant difference in the original and updated real and imaginary refractive indices occur across the TAFTS LW channel range. Given these differences, a spectrum simulated with ice particle scattering properties that incorporate the most recent refractive index values may differ from the spectrum presented in this paper. At some wavenumbers, less absorption will occur due to lower imaginary refractive index values, for example between 50 and 70 cm^{-1} and between 220 and 260 cm^{-1}. Across the TAFTS SW channel, the refractive indices do not differ. Updated single scattering properties are required to test the effect of the new ice refractive indices in a quantitative manner, since this could be important for comparing TAFTS LW spectra with simulated spectra.

5.4. Sensitivity to small ice crystals

Throughout this work it has been assumed that the 2DC cloud probe is correctly counting and sizing ice crystals between 25 and 100 μm. However, a number of studies report problems with the performance of the 2DC probe over this range (Baumgardner and Korolev, 1997; Strapp *et al.*, 2001). As the measured PSDs are modified to fit the simulated radiance to the infrared window region, such an effect should not impact the overall effective diameter representing the cirrus. However, if the wrong proportion of small (< 100 μm) ice is used in the PSDs, there is the possibility that the shape of the PSD will not be truly representative of the ice cloud. It was reported by Baran (2005) that the FIR is sensitive to PSD shape, and therefore the effect on the simulated FIR spectra of misrepresenting the small ice particles within the cirrus is investigated for this particular case-study.

A simulated spectrum has been produced using only 2DC probe measurements of ice greater than 100 μm. Ice crystals smaller than 100 μm were represented with the Field *et al.* (2005) parametrisation. The same fitting method as described in section 3.2 was performed using the aggregate

ice crystal to the infrared window region of the A_VOT_3 spectrum. In Figure 16 both the original fitted, and the modified PSDs are plotted for each of the cloud layers. There are significant differences in the PSDs for diameters less than 100 μm. In the upper three cloud layers, there are generally fewer small ice crystals than measured by the 2DC probe, indicating a potential problem with ice particles in the 2DC probe shattering into smaller pieces. The D_e for each of the modified PSDs from the upper to lower cloud layers is 20, 24, 27, and 35μm, compared with those for the original PSDs of 20, 23, 31 and 37μm. Although the particle sizes in each of the cloud layers do differ slightly, both spectra fulfill the fitting criteria used throughout this work. It has been shown that the FIR is not sensitive to particle size (Yang *et al.*, 2003), and so the spectral differences due to the PSD shape are likely to dominate over those due to particle size.

In Figures 17(a) and (b), the difference between the original simulated spectra and the latest simulated spectra are plotted over TAFTS LW and SW regions, respectively. There is little change in the simulated spectra over the TAFTS LW channel, with brightness temperature difference of up to 1.0 K. Over the TAFTS SW channel, the effect of disregarding the 2DC small ice produces a brightness temperature difference of 2.3 K at 330 cm^{-1} and this difference decreases towards higher wavenumbers. The representation of small ice is something that does have an impact on the FIR spectrum and illustrates the need for instrumentation to measure the small ice particles when doing a study such as this. However, the misrepresentation of small ice does not have a large enough effect to explain all the observed differences between the simulated and measured TAFTS spectra in this case, and at most wavenumbers is below the level of TAFTS uncertainty.

6. Conclusions

In this study, two sets of averaged TAFTS and ARIES upwelling spectra, measured at 10 km over cirrus with visible optical thickness between 0.1 and 0.3 were presented. Modelled spectra were produced using measured PSDs that were then modified by adding small ice particles (0–25 μm) and altering the total ice concentrations to produce agreement with observation in the infrared window region, so that a test of the consistency of modelling in both the MIR and FIR could be achieved. In modelling the cloud, differences were noted between the modelled and measured spectra above the level of instrument uncertainty in the FIR TAFTS LW and SW channels and also in the MIR. This pointed to the need for simultaneous measurements in both the FIR and window region to ensure that the correct PSDs and scattering properties are used when simulating cirrus radiative effects.

Sensitivity studies were performed to investigate the most likely cause of the disagreement between measured and modelled spectra. Four causes of uncertainty in modelling were identified and tested: RH profile within the cloud layer, boundary conditions to the cloud, crystal habit and small ice particle measurements. The RH profile was found to be likely to have an effect in LW microwindows but not in the SW region. The boundary conditions were not thought to affect the LW channel but contributed a significant uncertainty in the SW. For this case-study, any uncertainties due to crystal
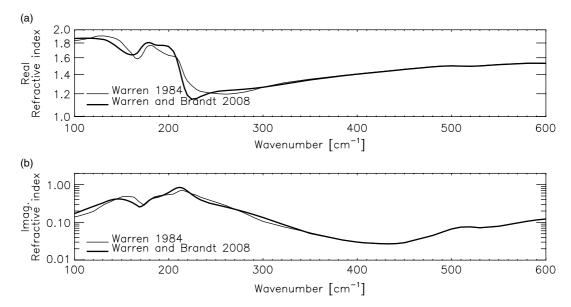
Figure 15. The two different compilations of (a) the real part and (b) the imaginary part of the refractive index of ice.
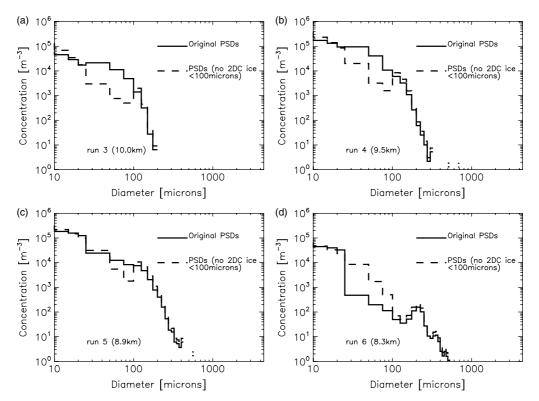

Figure 16. Particle size distributions which produced a fit to the ARIES infrared window region in each of the cloud layers at (a) 10 km, (b) 9.5 km, (c) 8.9 km, and (d) 8.3 km. The PSDs plotted in full lines use all 2DC data above 25 μm, and dashed lines use 2DC data only above 100 μm.

habit would not be detected above the instrument noise for the optically thin cirrus encountered on this flight. Studies of optically thicker cirrus would, however, produce more measurable effects for different crystal shapes at TAFTS wavelengths compared with the MIR. Finally, uncertainties in counting and sizing small particles would affect both the LW and SW regions most significantly between 230 and 420 cm^{-1} where the effect is comparable to the uncertainty of TAFTS spectral measurements. This demonstrates the need for accurate PSD shapes when simulating the FIR region.

This work has highlighted the need both for more high-resolution spectral measurements of cirrus in the far and mid infrared and for improved datasets. It is vital that the cloud is well sampled, particularly the small ice particles, and also the atmospheric water vapour profile. To reduce errors in modelling, cirrus with no underlying cloud is preferable. Also, to gain more sensitivity to ice crystal habit, an optically thicker cirrus case is needed.
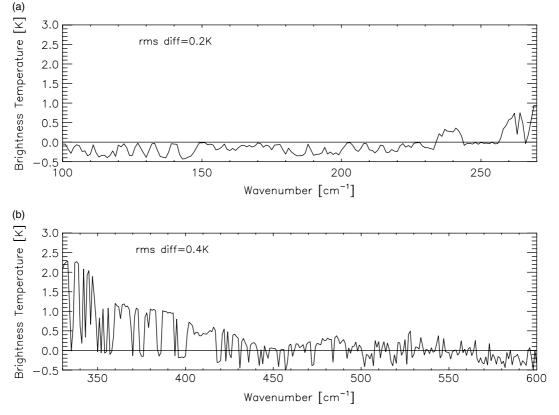
Acknowledgements

Figure 17. The differences between spectra simulated using the two sets of PSDs shown in Figure 16 for TAFTS (a) LW and (b) SW spectral regions.

References

Baker MB. 1997. Cloud microphysics and climate. *Science* **276**: 1072−1078.

Baran AJ. 2005. The dependence of cirrus infrared radiative properties on ice crystal geometry and shape of the size-distribution function. *Q. J. R. Meteorol. Soc.* **131**: 1129−1142.

Baran AJ, Francis PN. 2004. On the radiative properties of cirrus cloud at solar and thermal wavelengths: A test of model consistency using high-resolution airborne radiance measurements. *Q. J. R. Meteorol. Soc.* **130**: 763−778.

Baumgardner D, Korolev A. 1997. Airspeed corrections for optical array probe sample volumes. *J. Atmos. Oceanic Technol.* **14**: 1224−1229.

Brault JW. 1996. New approach to high-precision Fourier transform spectrometer design. *Appl. Opt.* **35**: 2891−2896.

Canas AA, Murray JE, Harries JE. 1997. The Tropospheric Airborne Fourier Transform Spectrometer. *Proc. SPIE* **3220**: 91−102.

Clough SA, Shephard MW, Mlawer E, Delamere JS, Iacono M, Cady-Pereira K, Boukabara S, Brown PD. 2005. Atmospheric radiative transfer modeling: a summary of the AER codes. *J. Quant. Spectrosc. Radiat. Transfer* **91**: 233−244.

Cox CV, Murray JE, Taylor JP, Green PD, Pickering JC, Harries JE, Last AE. 2007. Clear-sky far-infrared measurements observed with TAFTS during the EAQUATE campaign, September 2004. *Q. J. R. Meteorol. Soc.* **133**(S3): 273−283.

Cunningham RM. 1978. 'Analysis of particle spectral data from optical array (PMS) 1D and 2D sensors'. In *Proceedings of 4th Symposium on Meteorol. Obs. Instruments*. Denver: USA. Amer. Meteorol. Soc: Boston. 345−350.

Davis SP, Abrams MC, Brault JW. 2001. *Fourier Transform Spectrometry*. Academic Press: San Diego.

Field PR. 2000. Bimodal ice spectra in frontal clouds. *Q. J. R. Meteorol. Soc.* **126**: 379−392.

Field PR, Hogan RJ, Brown PR, Illingworth AJ, Choularton TW, Cotton RJ. 2005. Parametrization of ice-particle size distribution for midlatitude stratiform cloud. *Q. J. R. Meteorol. Soc.* **131**: 1997−2017.

Francis PN, Foot JS, Baran AJ. 1999. Aircraft measurements of the solar and infrared radiative properties of cirrus and their dependence on ice crystal shape. *J. Geophys. Res.* **104**(D24): 31685−31695.

Green PD. 2003. 'The development of a Fourier transform spectrometer to measure far-infrared fluxes in the upper troposphere'. PhD thesis. University of London.

Harries JE, Carli B, Rizzi R, Serio C, Mlynczak M, Palchetti L, Maestri T, Brindley H, Masiello G. 2008. The far-infrared Earth. *Rev. Geophys.* **46**: RG4004, DOI: 10.1029/2007RG000233.

Holz RE, Ackerman S, Antonelli P, Nagle F, Knuteson RO, McGill M, Hlavka DL, Hart WD. 2006. An improvement to the high-spectral-resolution CO2-slicing cloud-top altitude retrieval. *J. Atmos. Oceanic Technol.* **23**: 653−670.

Huang HL, Yang P, Wei H, Baum BA, Hu Y, Antonellis P, Ackerman A. 2004. Inference of ice cloud properties from high-spectral-resolution infrared observations. *IEEE Trans. Geosci. Remote Sensing* **42**: 842−853.

Knollenberg RG. 1976. The optical array: An alternative to scattering or extinction for airborne particle size determination. *J. Appl. Meteorol. Climatol.* **9**: 86−103.

Liou KN. 1986. Review. Influence of cirrus clouds on weather and climate processes: A global perspective. *Mon. Weather Rev.* **114**: 1167−1199.

Lynch DK, Sassen K, Starr DO, Stephens G (eds). 2002. *Cirrus*. Oxford University Press: Oxford, UK.

Newman SM, Knuteson RO, Zhou DK, Larar AM, Smith WL, Taylor JP. 2009. Radiative transfer validation study from the European AQUA Thermodynamic Experiment. *J. Quant. Spectrosc. Radiat. Transfer* **135**: 277−290.

NOAA, NASA, USAF. 1976. *US Standard Atmosphere 1976*. US Government Printing Office: Washington DC.

Rothman LS, Jacquemart D, Benner DC, Birk M, Brown LR, Carleer MR, Chackerian C, Coudert LH, Dana V, Devi VM, Flaud JM, Gamache RR, Goldman A, Hartmann JM, Jucks KW, Maki AG, Mandin JY, Massie ST, Orphal J, Perrin A, Rinsland CP, Smith MAH, Tennyson J, Tolchenov RN, Toth RA, Vander Auwera J, Varanasi P, Wagner G. 2005. The HITRAN 2004 molecular spectroscopic database. *J. Quant. Spectrosc. Radiat. Transfer* **96**: 139−204.

Seinfeld JH, Pandis SN. 1998. *Atmospheric Chemistry and Physics*. John Wiley and Sons: New York.

Sinha A, Harries JE. 1995. Water vapour and greenhouse trapping: The role of far-infrared absorption. *Geophys. Res. Lett.* **32**: 2147−2150.

Stamnes K, Tsay S, Wiscombe W, Jayaweera K. 1988. Numerically stable algorithm for discrete-ordinate-method radiative transfer in multiple scattering and emitting layered media. *Appl. Opt.* **27**: 2502−2509.

Strapp JW, Albers F, Reuter A, Korolev AV, Maixner U, Rashke E, Vukovic Z. 2001. Laboratory measurements of the response of a PMS OAP-2DC. *J. Atmos. Oceanic Technol.* **18**: 1150−1170.

Thorne AP, Litzen U, Johansson S. 1999. *Spectrophysics, Principle and Applications*. Springer: Berlin.

Turner DD. 2005. Arctic mixed-phase cloud properties from AERI lidar observations: Algorithm and results from SHEBA. *J. Appl. Meteorol. Climatol.* **44**: 427–444.

Warren SG. 1984. Optical constants of ice from the ultraviolet to the microwave. *Appl. Opt.* **23**: 1206–1225.

Warren SG, Brandt RE. 2008. Optical constants of ice from the ultraviolet to the microwave: A revised compilation *J. Geophys. Res.* **113**: D14220.

Wilson SHS, Atkinson NC, Smith JA. 1999. The development of an airborne infrared interferometer for meteorological sounding studies. *J. Atmos. Oceanic Technol.* **18**: 2003–2012.

Yang P, Mlynczak MG, Wei H, Kratz DP, Baum BA, Hu YX, Wiscombe WJ, Heidinger A, Mishchenko MI. 2003. Spectral signatures of ice clouds in the far-infrared region: Single-scattering calculations and radiative sensitivity study. *J. Geophys. Res.* **108**: 4569–4584.

Zhang Y, Macke A, Albers F. 1999. Effect of crystal size spectrum and crystal shape on stratiform cirrus radiative forcing. *Atmos. Res.* **52**: 59–75.